Materials Horizons

ROYAL SOCIETY OF CHEMISTRY

COMMUNICATION

View Article Online
View Journal | View Issue

Cite this: *Mater. Horiz.*, 2025, **12**, 6812

Received 24th February 2025,
Accepted 21st May 2025

DOI: 10.1039/d5mh00335k

rsc.li/materials-horizons

Charge carrier transport in two-dimensional benzimidazole-based perovskites†

Shuanglong Wang,[a] Lei Gao,[a] Mukunda Mandal,[a] Hao Wu,[a] Zhitian Ling,[a] Mischa Bonn,[a] Denis Andrienko,[a] Paul W. M. Blom,[a] Hai I. Wang,[ab] Wojciech Pisula *[ac] and Tomasz Marszalek *[ac]

Two-dimensional (2D) perovskites have emerged as promising candidates for field-effect transistors (FETs) due to their pronounced stability in the presence of insulating bulky organic spacer cations. However, the underlying mechanism of the charge carrier transport in these 2D perovskite semiconductors remains elusive. In this study, the temperature dependence of the charge carrier properties of benzimidazolium tin iodide perovskite ($(Bn)_2SnI_4$) is studied to evaluate the corresponding transport mechanism on nanoscopic and macroscopic dimensions. By combination of solvent engineering to optimize the morphology of perovskite thin films and choice of the organic imidazole-based spacer inducing hydrogen bonding with the inorganic $[SnI_6]^{4-}$ octahedron layer, less ionic defects are generated resulting in suppressed ion movement. It was possible to separate the influence of mobile ions and temperature on the charge carrier transport in transistors. The decline of the charge carrier mobility with temperature decrease in the device indicates a hopping mechanism for macroscopic transport. On the other hand, the local charge transport was determined by ultrafast terahertz photoconductivity measurements revealing an increasing mobility to 17 $cm^2\ V^{-1}\ s^{-1}$ with temperature decrease implying a band mechanism on the nanoscopic scale. The local charge carrier mobility is associated with the particularly regular structure of the octahedral $[SnI_6]^{4-}$ sheets induced by symmetric hydrogen bonding with the benzimidazolium cation. Our results provide key insights on the charge transport properties of perovskite semiconductors, which have important implications for realizing high-performance electronic devices.

New concepts

Two-dimensional (2D) hybrid organic–inorganic metal halide perovskites with incorporated large A-site organic cations offer enhanced stability and structural diversity, making them promising for optoelectronics applications. Nevertheless, the performance of 2D perovskites-based devices is still limited due to defect related ion migration resulting in poor charge carrier transport. As a new concept a benzimidazolium cation was incorporated into tin iodide perovskite to reduce structural defects and to enhance the performance of field-effect transistors. In combination with optimized solution processing from mixed solvents, corresponding field-effect transistors show improved hysteresis behavior due to lowered ion migration. Symmetric hydrogen bonding with the benzimidazolium cation ensures a regular structure of the octahedral $[SnI_6]^{4-}$ sheets which is important for the chare carrier transport. For this reason, an effective band mechanism at the local scale has been identified through ultrafast terahertz photoconductivity measurements, which indicate charge carrier mobilities of 17 $cm^2\ V^{-1}\ s^{-1}$. This work provides a fundamental understanding on the charge transport properties of 2D perovskites and contributes towards high-performance optoelectronic devices.

Introduction

Metal halide perovskites as new-generation semiconducting materials have been widely applied in various optoelectronic devices due to their low-cost solution processibility and attractive electronic properties, such as high intrinsic charge mobility.[1–3] Field-effect transistors (FETs), as an important electronic element in logic circuits, serve as a valuable platform to study the charge transport of semiconductors and provide comprehensive insights into the electrical properties of perovskite materials. Despite recent progress in the development of perovskite FETs, devices still suffer from limited reliability and poor operational stability at room temperature.[4] These limitations are related to severe ion migration and accumulation at electrode interfaces under applied external voltage. These effects result in the shielding of the electric fields and weak gate modulation of the FETs.[5] Consequently, the devices

[a] *Max Planck Institute for Polymer Research, Ackermannweg 10, 55128 Mainz, Germany. E-mail: pisula@mpip-mainz.mpg.de, marszalek@mpip-mainz.mpg.de*
[b] *Nanophotonics, Debye Institute for Nanomaterials Research, Utrecht University, Princetonplein 1, 3584 CC, The Netherlands*
[c] *Department of Molecular Physics, Faculty of Chemistry, Lodz University of Technology, Zeromskiego 116, 90-924 Lodz, Poland*

† Electronic supplementary information (ESI) available. See DOI: https://doi.org/10.1039/d5mh00335k

typically exhibit low field-effect mobility and pronounced dual-sweep hysteresis, unfavorable for practical applications.[6]

To address these issues, various approaches such as using perovskite single crystals,[7] high-k gate dielectric layer,[8] doping,[9] and others[10] have been explored. Among these attempts, dimensionality engineering by employing two-dimensional (2D) Ruddlesden–Popper layered perovskites with a chemical formula of $(RNH_3)_2BX_4$ has been considered an effective way to suppress ion movement through the incorporation of insulating bulky cations into the perovskite structure. In the formula, R, B, and X are long alkyl chains or aromatic spacer cations, divalent metallic cations, and halide anions, respectively.[11,12] Previous studies have identified tin and iodide elements at the B- and X-site for FET applications thanks to their smaller in-plane effective mass and reduced Fröhlich effect.[13,14] In this regard, the structure engineering of the spacer allowed to enhance the device performance of the 2D layered perovskites FETs. Normally, the A-site spacer cations in 2D layered perovskites do not contribute directly to the density of states at the band edge, which originates mainly from the B- and X-site components.[15] Nevertheless, the steric strain induced by the organic ligands imposed on the metal–halide octahedra reduces ion migration and influences the optoelectronic properties of the 2D layered perovskites.[16] To date, a single-ring aromatic cation, *e.g.* phenethylammonium (PEA), has been extensively investigated in 2D perovskite FETs, and a few groups also studied quaterthiophene-based ligands.[17,18] We have recently introduced 2-thiopheneethylammonium and linear alkyl cations into 2D tin perovskites and demonstrated their application in FETs.[11,19]

Despite the recent progress on 2D tin perovskite FETs, most studies mainly focus on optimizing device mobility at room temperature, with little effort in unveiling the temperature effects on charge transport behavior which can provide important insights on the charge carrier transport mechanism in perovskite semiconductors. More importantly, ion migration is known to be thermally activated and can be reduced or even suppressed upon decreasing the operating temperature.[21] So far, the charge transport in three-dimensional perovskites has been widely investigated by temperature-dependent FET measurements.[22] Unfortunately, a corresponding systematic investigation of 2D layered tin halide perovskites is still rare, impeding a fundamental understanding of their charge transport properties in the FET configuration especially in correlation to their inherent mechanism.

Recently, benzimidazolium-based organic cations have been synthesized for perovskite applications. Compared to other reported organoammonium cations terminated by alkyl–NH_3^+ groups, the hydrogen bond between imidazole-based cations and the metal-halide octahedral sheets is more symmetrical, which is expected to reduce the distortion of the inorganic octahedral of the 2D perovskite structure as a distinct pathway for the charge carriers.[23] For example, Dyksik and coworkers demonstrated the broad tunability of carrier effective masses in 2D halide perovskites through the choice of the organic templating layer and metal cations based on the experimental results with electronic band-structure calculations.[24] Additionally, Peksa *et al.* showed that 2D perovskites containing benzotriazole-based organic cation has the lowest reduced effective mass among lead iodide 2D perovskites. The low reduced effective mass was attributed to a low degree of octahedral distortion.[25] These findings disclose that a higher degree of ordering of the octahedral units is expected to reduce the effective mass of the charge carriers. Therefore, benzimidazolium (Bn) was selected as an organic spacer for this work to study the crystal structure, film morphology and charge carrier transport of the tin iodide based perovskite, $(Bn)_2SnI_4$. The charge carrier transport in the $(Bn)_2SnI_4$ perovskite was investigated at both nano- and macroscopic scales across various temperatures. Ultrafast terahertz photoconductivity results reveal high charge carrier mobilities up to 17 $cm^2\ V^{-1}\ s^{-1}$ and indicate an unhindered band transport which is attributed to the regular structure of the octahedral $[SnI_6]^{4-}$ sheets as proven by density functional theory calculations. As consequence of the improved film morphology obtained from mixed solvent and possibly the ordered inorganic octahedron layers, less ionic defects are formed and the ion migration in FETs is drastically suppressed. However, the decline of the charge carrier mobility with temperature decrease in the device implies a hopping mechanism for the macroscopic transport. The change from band to hopping transport is related to structural defects and domain boundaries on the macroscopic scale. Our findings provide important insights into the charge transport properties of 2D tin halide perovskites in FETs.

Results and discussion

The chemical structure of the Bn cation is presented in Fig. 1(a). To better understand the effects of this cation as an organic spacer on the octahedral $[SnI_6]^{4-}$ inorganic sheets, the electronic properties of the 2D perovskite semiconductor $(Bn)_2SnI_4$ were evaluated employing density functional theory (DFT) calculations (see the Experimental section for computational details). The DFT calculations reveal a distance of 14.8 Å between adjacent inorganic layers. The distortion of the inorganic framework is assessed by the Sn–I bond lengths and Sn–I–Sn bond angles. As shown in Fig. S1 (ESI†), the average bond angle is close to the ideal angle of 180°. Meanwhile, the small variation of Sn–I bond lengths indicates regular inorganic skeletons. These indicate that the 2D $(Bn)_2SnI_4$ perovskite is expected to be beneficial as a potential channel material for charge carrier transport. Fig. 1(b) illustrates the electronic band structure of $(Bn)_2SnI_4$ along high symmetry points within the first Brillouin zone, revealing that both the valence band maximum (VBM) and the conduction band minimum (CBM) occur at the Y-point (0.0, 0.5, 0.0), suggesting a direct band gap with a calculated band gap of 1.64 eV. Hole effective masses (m_h^*) are determined relative to the rest mass of free electrons (m_0) through fitting the band edges with a third-order polynomial, resulting in a value of −0.196 ($Y \rightarrow \Gamma$), which was later utilized to evaluate the hole mobility in the subsequent THz analysis. With respect to the hole effective masses, the electron

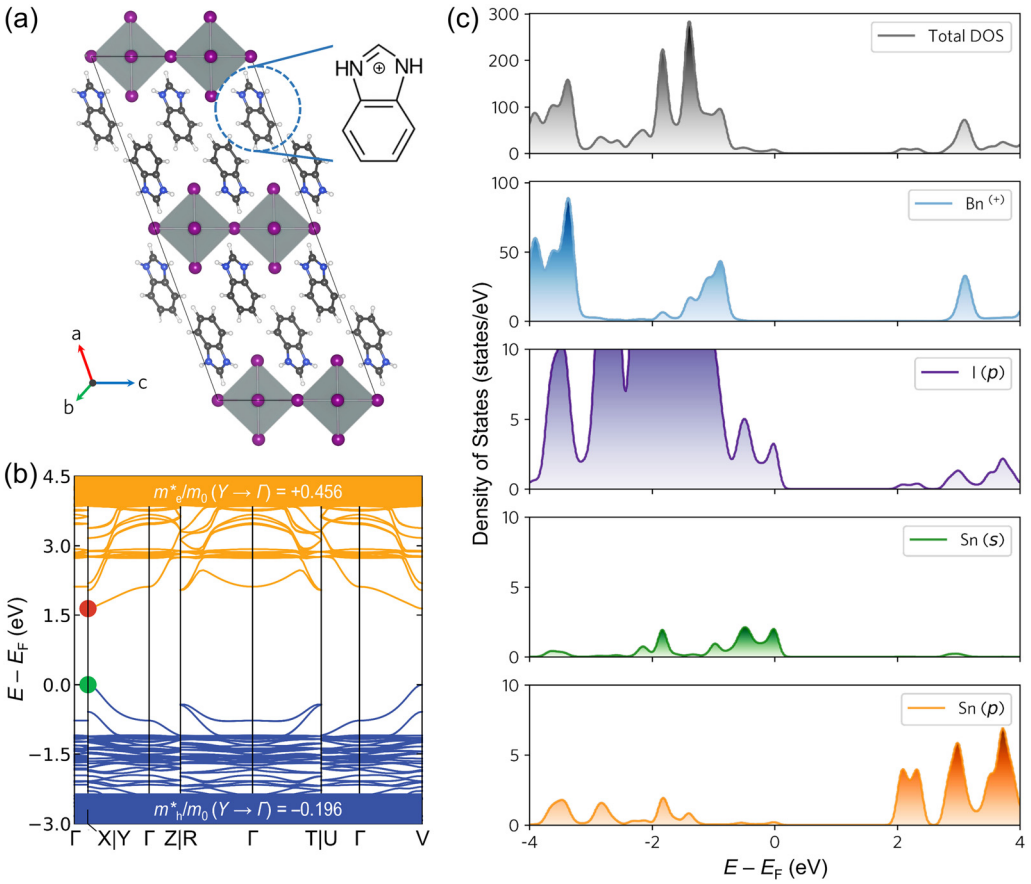

Fig. 1 (a) Illustration of DFT-optimized crystal structure of the layered perovskite $(Bn)_2SnI_4$, along with the chemical structure of the benzimidazole (Bn) cation. (b) The band structure and (c) densities of states (DOS) plots for $(Bn)_2SnI_4$ derived from DFT calculations. The effective mass of holes and electrons (m^*_h/m^*_e) is reported in the units of the free electron rest mass (m_0 = 9.11 × 10^{-31} kg).

effective masses (m^*_e) are significantly larger (Fig. 1(b)), yielding a value of +0.456 ($Y \rightarrow \Gamma$). The calculated total and projected densities of states (DOS and pDOS, respectively) for $(Bn)_2SnI_4$ are presented in Fig. 1(c). Consistent with the behavior observed in other Sn-based 2D perovskites, the Sn 5s and I 5p orbitals emerge as the primary contributors to the VBM in $(Bn)_2SnI_4$, with the I 5p orbital making the larger contribution.[17] In contrast, the principal contributors to the CBM are Sn 5p and I 5p orbitals, with the metal-based orbital playing a more pronounced role. To evaluate the influence of the organic spacer, the partial DOS contributions originating from C, H, and N atoms were investigated. Summing up these contributions and plotting them (blue curve) allowed us to disentangle the independent contribution of the organic layer. These results indicate that the organic layer does not have a "direct" impact on the electronic properties of $(Bn)_2SnI_4$, as its contribution remains distinct from both VBM and CBM.

Improved morphology and crystallinity in polycrystalline perovskite thin films are prerequisites for facilitating charge transport.[26] The processing solvent plays an important role in controlling the crystallization kinetics of perovskite films. To fine-tune the crystallization of the $(Bn)_2SnI_4$ films, dimethyl sulfoxide (DMSO) and dimethylacetamide (DMAC) were mixed with *N*,*N*-dimethylformamide (DMF) forming mixed DMF : DMSO and DMF : DMAC solvent systems. DMF is the most widely used solvent to prepare perovskite precursor solutions. DMF has a relatively low Gutmann donor number of 26.6 kcal mol^{-1} compared to DMSO and DMAC, with 29.8 and 27.8 kcal mol^{-1}, respectively.[27] A solvent with a high Gutmann number strongly coordinates with divalent metal centers and suppresses the formation of molecular clusters.[28,29] As a result, DMF-based films show rough morphology with a large number of pinholes, which is detrimental to long-range charge transport.[30] The boiling point is another key parameter to determine the evaporation rate of the solvent. It has been reported that the polar solvent DMSO with a high boiling point of 189 °C is less volatile and can readily remain in the perovskite film even after thermal annealing.[31] The residual solvent in the film can decrease the crystallinity, leading to reduced film quality. On the contrary, DMF and DMAC with low polarity, which have a low boiling point of 152 °C and 165 °C, respectively, are more volatile during annealing.[31] Within the optimization of the deposition process, the mixing ratio of DMF : DMSO and DMF : DMAC of 4 : 1 showed the highest crystallinity and improved film morphology and therefore this mixed solvent was chosen for film deposition. The effects of processing solvents on the perovskite

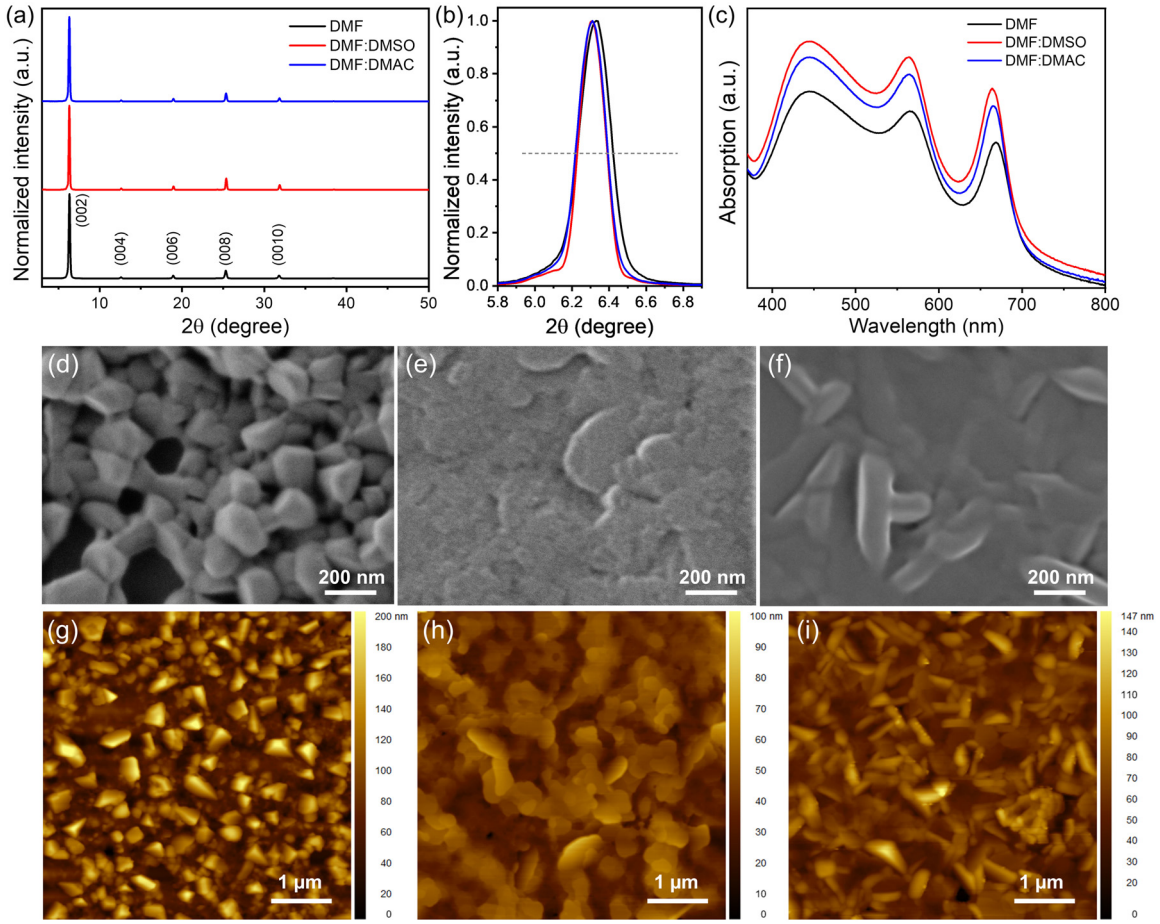

Fig. 2 (a) Out-of-plane XRD of $(Bn)_2SnI_4$ films cast from different solvents. (b) FWHM analysis of the (002) peak. (c) UV-vis absorption of the three perovskite films. SEM and AFM images for the $(Bn)_2SnI_4$ films processed from different solvents of (d) and (g) DMF; (e) and (h) DMF : DMSO; and (f) and (i) DDF : DMAC, respectively.

crystal structure were first studied by X-ray diffraction (XRD). The XRD patterns demonstrate that the well-organized layered structure can be easily formed for $(Bn)_2SnI_4$ perovskite (Fig. S2, ESI†). Fig. 2(a) shows the X-ray diffractograms (XRD) of the $(Bn)_2SnI_4$ thin films processed from pure DMF, DMF : DMSO and DMF : DMAC solvents and annealed at a temperature of 100 °C. To ensure comparison, the thickness of the films was kept at 30 nm (Fig. S3, ESI†). These three samples exhibit typical (00*l*) out-of-plane organization (l = 2, 4, 6, 8, and 10), indicating the formation of a layered structure.[32] From the position of the (002) diffraction peak at 6.29° an interlayer distance of 14.1 Å is found for the three films, which matches well with the DFT calculations. The above result confirms that the optimized solvent mixtures do not affect the crystal lattice in the layered perovskite structure. In addition, the full width at half maximum (FWHM) of the (002) crystal facet is 0.2°, 0.15°, and 0.17° for films obtained from pure DMF, DMF : DMSO and DMF : DMAC, respectively, suggesting slightly improved out-of-plane crystallinity of the film with the mixed solvents compared to the pure DMF (Fig. 2(b)).[33]

The UV-vis absorption spectra of the $(Bn)_2SnI_4$ perovskite films cast from the three different solvent systems are compared in Fig. 2(c). The three films show similar absorption features in the visible spectral range. The sharp peak at 668, 663, and 665 nm for pure DMF, mixed DMF : DMSO, and DMF : DMAC processed films are characteristic of intrinsic excitonic absorption due to the dielectric confinement effect, demonstrating the layered quantum well structure of the perovskite.[34] The similar position of the excitonic peak suggests an identical structure of the perovskite films.[35] But the higher steady-state photoluminescence (PL) intensities of the film obtained from mixed solvents indicate less defects and higher crystallinity (Fig. S4, ESI†).[19] The morphologies of the three perovskite films were further studied by scanning electron microscopy (SEM) and atomic force microscopy (AFM) characterizations. As shown in Fig. 2(d)–(i), when processed from pure DMF solution, pinholes and grains of varied sizes are formed in the $(Bn)_2SnI_4$ film, leading to a rough film surface with a high root-mean-square (RMS) roughness of 34.4 nm. The poor film morphology with the pinholes is responsible for large boundaries limiting the charge transport in the film. On the contrary, processed from mixed solvents, the $(Bn)_2SnI_4$ films exhibit a more uniform and smooth morphology with improved surface coverage. As a consequence, the RMS values are reduced to 14.6 and 18.9 nm for films obtained from DMF : DMSO and DMF : DMAC,

respectively. The improved morphology is related to the beneficial role of DMSO and DMAC as discussed above in tuning the crystallization process of the $(Bn)_2SnI_4$ perovskite films (Fig. 2(h) and (i)). It should be noticed that in comparison to DMF and DMF : DMSO processed films, DMAC induces changes in the grain shape from rounded to nanorods and nanoplates. We attribute the morphological variations to the aforementioned different crystallization kinetics with these solvents.

To investigate the charge carrier transport of these three perovskite films deposited from different solvents, FETs were fabricated with bottom-gate/top-contact configuration (Fig. 3(a)). The transfer curves were recorded at $V_{ds} = -60$ V with V_g scanned from +60 to −60 V in pulse mode. The electrical characteristics were measured in vacuum under dark conditions to avoid the degradation of perovskites (see more details in the Experimental Section). Fig. 3(b) and (c) show the summarized electrical parameters, including charge carrier mobility, threshold voltage (V_{th}), on/off current ratio ($I_{on/off}$), and subthreshold swing (SS) recorded at 295 K for the films obtained from different solvents. All parameters are extracted from the saturation region of the transfer curve in the forward direction. The transfer curves of all $(Bn)_2SnI_4$ FETs exhibit typical p-channel characteristics. The pristine device processed from pure DMF shows an average field-effect mobility, V_{th}, $I_{on/off}$, and SS value of 0.08 $cm^2\ V^{-1}\ s^{-1}$, 7 V, $\sim 10^2$, and 20 V dec^{-1}, respectively (Fig. 3(d)). On the other hand, the FETs obtained from the co-solvents reveal improved overall performance. The devices from DMF : DMSO and DMF : DMAC reveal higher charge carrier mobility of 0.26 and 0.15 $cm^2\ V^{-1}\ s^{-1}$, as shown in Fig. 3(e) and (f). It is worth noting that at 295 K the output characteristics of the devices from mixed solvents in Fig. 3(h) and (i) are also improved compared to the pristine device, which both additionally show a relatively good gate modulation of the channel current (Fig. 3(g)). Additionally, the bias stress stabilities for the $(Bn)_2SnI_4$ perovskite FETs based on different solvents are summarized in Fig. S5 (ESI†). The normalized source–drain current ($I_{ds}(t)/I_{ds}(0)$) of the $(Bn)_2SnI_4$ FETs with DMF : DMSO and DMF : DMAC solvents degrades slower than the pristine device, further confirming the beneficial role of the solvent mixture in improving the device bias stability by effectively reducing defects and lowering ion migration as further discuss in the following.

To deeper analyze the transport mechanism, in the first step the trap density number (N_t) at the dielectric/perovskite interface was evaluated on the basis of the SS values as defined by the following equation: $SS = \frac{k_B T \ln 10}{q}\left[1 + \frac{q^2}{C_i} N_t\right]$, with k_B the Boltzmann constant; T the absolute temperature; q the elementary charge and C_i the areal capacitance of the dielectric layer.[36]

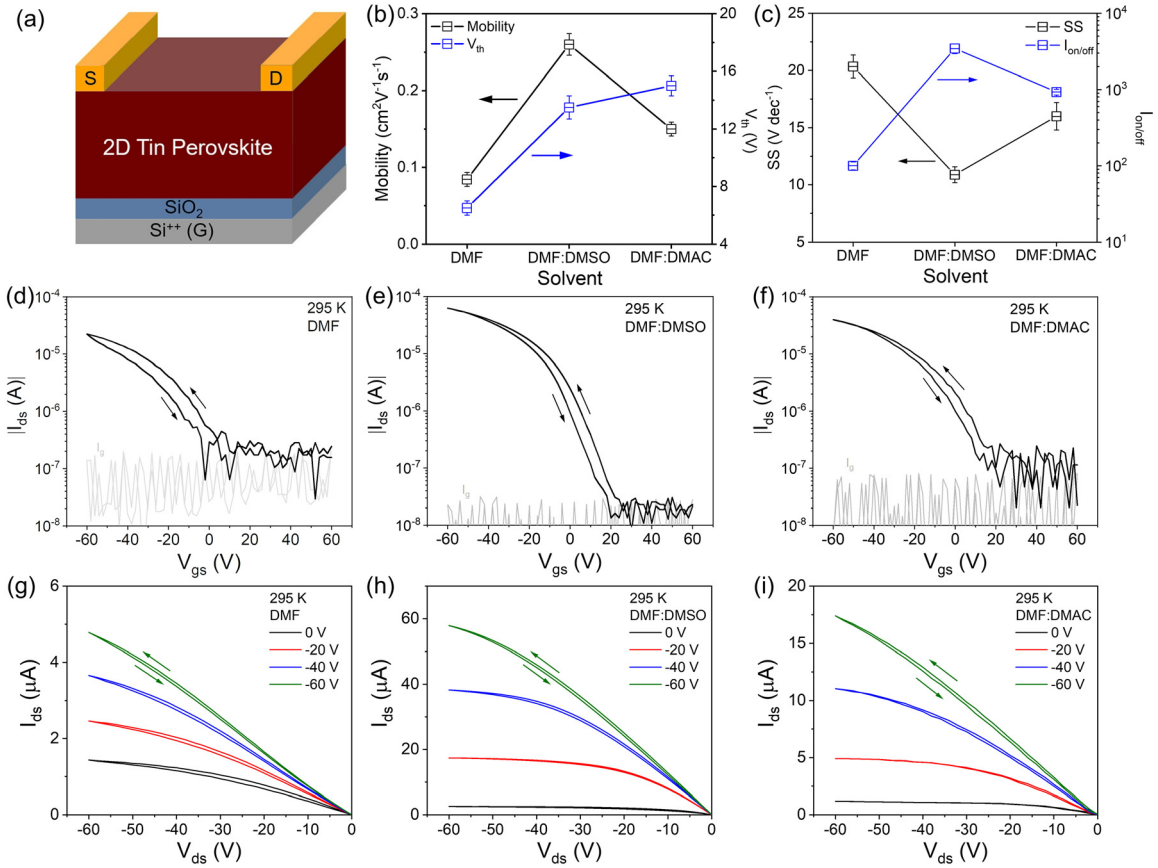

Fig. 3 (a) Top-contact bottom-gate structure of $(Bn)_2SnI_4$ FETs. Summary of (b) charge carrier mobility and V_{th}, and (c) SS and $I_{on/off}$ for $(Bn)_2SnI_4$ FETs fabricated from different solvents. The error bars were calculated from 10 individual devices. Transfer and output curves of the devices at 295 K processed from (d) and (g) pure DMF, (e) and (h) DMF : DMSO, and (f) and (i) DMF : DMAC, respectively.

We found that N_t decreases from 2.5 × 10^{13} cm^{-2} eV^{-1} for the pristine DMF $(Bn)_2SnI_4$ FET to 1.1 × 10^{13} and 1.6 × 10^{13} cm^{-2} eV^{-1} for the DMF : DMSO and DMF : DMAC processed FETs. These results suggest that the solvent mixtures improve the film quality at the perovskite/dielectric interface contributing to lower SS and reduced trap density. The FETs based on mixed solvents also show reduced dual-sweep hysteresis. The ΔV_g parameter, which is assigned to the V_g difference in both forward and backward sweep directions at $|I_{ds}|$ = 10^{-6} A (around halfway between the on and off states), is defined to quantitatively analyze the hysteresis of the FET devices.[37,38] The pristine device reveals a ΔV_g of 8.5 V, which decreases to 5.5 and 5.3 V for the mixed solvents. The lowered hysteresis can be attributed to a combination of suppressed ion migration and reduced interface defects.[39] Since the 2D $(Bn)_2SnI_4$ perovskite films based on the co-solvents provide higher crystallinity and enhanced morphologies, the density of defects decreases, leading to lower ion movement. Through appropriate solvent tuning, the effects of ionic screening can be reduced and improved transistor characteristics are obtained.

It should be noted that both reference and optimized $(Bn)_2SnI_4$ exhibited suppressed hysteresis compared to other 2D tin halide perovskite FETs based on alkyl–NH_3^+ terminal incorporated organic spacers, such as PEA,[13] phenylpropylammonium (PPA),[17] 2-thiopheneethylammonium (TEA),[19] and butylammonium (BA).[20] Since the hysteresis of perovskite FETs at room temperature is closely related to the ion migration and accumulation process, a lowering of the hysteresis indicates reduced ionic defects in the $(Bn)_2SnI_4$ thin films.

To further elucidate the charge transport mechanism in the $(Bn)_2SnI_4$ films, temperature-dependent FET measurements were conducted for a temperature range from 90 to 295 K. Generally, the effect of ion migration in perovskite FETs can be mitigated to a great extent by operating the devices at low temperature wherein the ions are believed to be immobilized.[11] This study allows the investigation of charge transport behavior in perovskite semiconductors in the absence of ion accumulation. Fig. 4(a)–(c) shows the transfer characteristics of $(Bn)_2SnI_4$ FETs processed from different solvents for different operation temperatures. The corresponding other electrical parameters and the output curves at low temperature are summarized in Fig. S6 and S7 (ESI†). For all three deposition conditions, the hysteresis completely disappears in the transfer curves at a temperature of around 200 K (Fig. 4(d)–(f)). This behavior is attributed to suppressed ion migration in the low-temperature regime. In comparison, hybrid tin perovskites, that contain phenylalkylammonium cations with odd carbon-numbered spacer and reveal a twisted octahedron framework, result in more severe ion migration also at low temperatures.[17,40] The conjugated imidazole Bn organic spacer induces stronger hydrogen bonding interactions with the inorganic $[SnI_6]^{4-}$ octahedron layer possibly leading to less ionic defects. Since ion migration is suppressed, the increase in charge carrier mobility from 90 to 200 K is solely attributed to a thermally activated transport and hopping mechanism.[41]

Ultrafast terahertz (THz) photoconductivity measurements were performed to complement electrical transport measurements. Unlike the electrical measurements of FETs, where long-range charge transport effects are studied, the THz probe reports the local, intrinsic charge carrier mobility in the spatial range of ~10 nm due to the transient nature of the THz pulse (with ~1–2 ps duration).[42] Our findings unveil a dichotomy in charge conduction mechanisms of $(Bn)_2SnI_4$ films obtained from the DMF : DMSO mixture. Fig. 5(a) and (b) show the temperature-dependent product of the mobility (μ) and free carrier generation quantum yield (ϕ) and the corresponding extracted peak values of mobility. Interestingly, we observe that photoconductivity increases with lowering temperature and reaches a high mobility up to ~17 cm^2 V^{-1} s^{-1}. By fitting with the equation followed by $\mu \propto T^{-\beta}$(1), β = 0.65 is extracted as

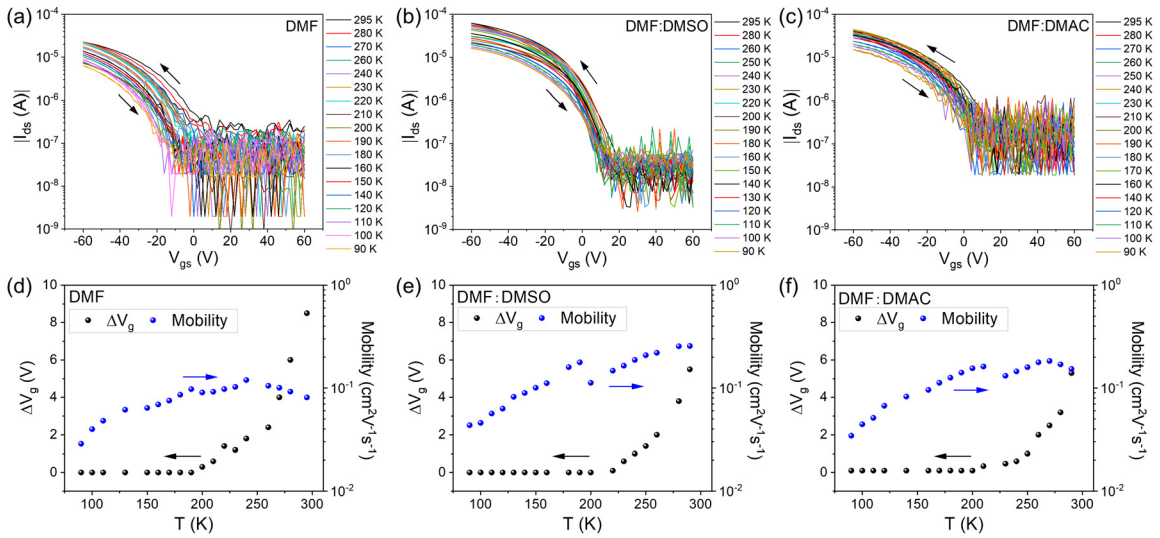

Fig. 4 Temperature-dependent transfer characteristics of the $(Bn)_2SnI_4$ FETs prepared from (a) pure DMF, (b) DMF : DMSO, and (c) DMF : DMAC. The corresponding temperature dependence of (d)–(f) hysteresis and charge carrier mobility for the three FET devices.

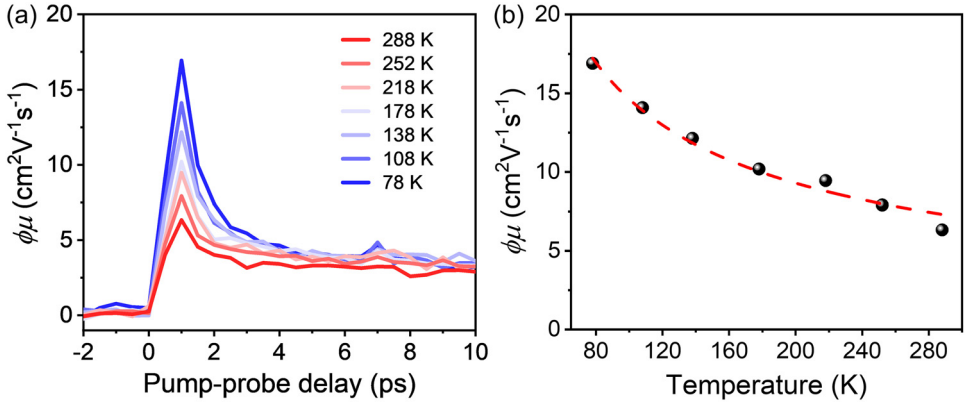

Fig. 5 (a) Temperature-dependent terahertz photoconductivity measurements of a $(Bn)_2SnI_4$ thin film prepared from mixed DMF : DMSO solvent. Temperature-dependent OPTP dynamics at fixed pump fluence reveal enhanced mobility at lower temperatures. (b) Charge carrier mobility as a function of temperature. The red dashed line is the fitting result following $\mu \propto T^{-\beta}$.

shown by the red dashed line in Fig. 5(b). We note that the estimated mobility here represents the lower limit of charge carrier mobility as we assume a unity free-carrier generation quantum yield (ϕ = 100%) in the sample. These results indicate that the short-range, intra-grain transport is governed by band-like conduction mechanism, drastically different from the thermally activated charge transport on the macroscopic scale in FET devices. We attribute the difference in temperature-dependent charge transport behavior in THz spectroscopy and transistors to their different working mechanisms.[17] The pronounced intrinsic charge carrier transport with the corresponding band mechanism has been already observed for few other 2D and 3D perovskites,[42–44] whereby the local charge carrier mobility of 17 cm^2 V^{-1} s^{-1} is related to the high regularity of the inorganic framework of $(Bn)_2SnI_4$ which is established by the symmetric hydrogen bonds between imidazole-based cations and the metal-halide octahedral sheets (Table S1, ESI†). In contrast, in FET devices, charge carriers drift over the micrometer range in the channel through multiple perovskite domain boundaries and structural defects along the applied electric field. Due to charge trapping at these structural inhomogeneities the transport is dominated by a hopping mechanism.[42] The combined THz and FET results suggest that, although the current device demonstrates reasonable performance, further processing optimization to grow film morphologies with larger domains and lower defect density will enable higher charge carrier mobility (*e.g.* >10 cm^2 V^{-1} s^{-1}) in perovskite transistors in the future.

Conclusions

We studied the charge transport properties of 2D $(Bn)_2SnI_4$ perovskite by FET and high-frequency THz spectroscopy. The benzimidazole cations establish symmetric hydrogen bonds with the octahedral $[SnI_6]^{4-}$ sheets in the perovskite ensuring a regular structure of the inorganic layers. The order of the octahedral sheets may contribute to an efficient local charge carrier transport up to 17 cm^2 V^{-1} s^{-1} that is assigned to a band mechanism. The crystallization and morphology of the $(Bn)_2SnI_4$ perovskite film are optimized through rational solvent engineering, promoting the p-type device performance of the FETs. The analysis of the device behavior proved a significant suppression of the ion migration which is attributed to reduced ionic defects due to improved film morphology and probably also the ordered octahedral sheets. The increase of the charge carrier mobility with increasing operation temperature of the FET from 90 K to 295 K is characteristic for a thermally activated transport and hopping mechanism. Structural defects and domain boundaries act as trapping sites and dominate the hopping mechanism for the macroscopic charge transport resulting in reduced mobilities in comparison to the efficient transport at the nanoscopic scale. The insights of this study emphasize the importance of the structural order and film morphology of perovskite semiconductors for the performance of electronic devices.

Experimental section

Materials

All the chemicals were used as received without any other refinement unless otherwise specified. Benzimidazol (99.8%), tin(II) iodide (SnI_2, 99.999%), *N*,*N*-dimethylformamide (DMF, anhydrous, 99.8%), dimethyl sulfoxide (DMSO, anhydrous, ≥99.9%), and dimethylacetamide (DMAC, anhydrous, ≥99.8%) were purchased from Sigma-Aldrich. Heavily doped Si/SiO_2 (300 nm) substrates were obtained from Ossila Ltd.

Synthesis of organic salt benzimidazolium iodide (BnI)

Precursor benzimidazole (2.36 g, 20 mmol) was dissolved in aqueous HI solution (57%, 8 ml, ~30 mmol of HI) in a round-bottom flask. The solution was cooled down to 0 °C in an ice bath and then left to react for 3 h, and then slowly warmed up to room temperature. Then the reaction was stopped, and the solvent was removed using a rotary evaporator, and the residue was further washed with diethyl ether for several times. The washed solid was redissolved in EtOH and recrystallized by

adding diethyl ether. The recrystallized solid was filtered and washed by diethyl ether for three times. After drying in a vacuum oven overnight at room temperature, the solid organic salt BnI was obtained (Fig. S8 and S9, ESI†). ^{1}H NMR (400 MHz, DMF) δ 9.62 (s, 1H), 7.88 (t, 2H), 7,63 (t, 2H). ^{13}C NMR (101 MHz, DMF) δ 141.23, 131.07, 126.44, 114.73.

FET fabrication

Bare Si/SiO_2 wafers were cleaned in ultrasonication bath with acetone and isopropanol for 30 min in a sequential manner. After drying by flowing nitrogen, the substrates were treated with UV/ozone for 20 min then transferred into a glove box for further use. The perovskite precursor solution with the concentration of 0.1 M was prepared by dissolving the organic salt BnI and SnI_2, with molar ratio of 2 : 1 in pure DMF, mixed DMF/DMSO (4 : 1) and DMF/DMAC (4 : 1), respectively. Then the solution kept stirring for 2 h at room temperature in N_2 glovebox and filtered with a 0.2 μm polytetrafluorethylene filter before use. Perovskite thin films were deposited by spin coating the solution at 4000 rpm for 60 s, followed by thermal annealing at 120 °C for 10 min on a hotplate. Finally, source and drain electrodes with 80 nm gold were thermally evaporated through a shadow mask for 80 × 1000 μm (length × width) transistor channels.

Thin film characterization

The optical absorption spectra of perovskite films were measured using an UV/Vis spectrophotometer from a PerkinElmer Lamda 25 instrument with an all-reflecting, double-monochromator optical system and holographic gratings used in each monochromator for the UV-vis range. During all measurements, the samples were kept in the air and at room temperature. The steady PL spectra were measured using VANTES SenseLine spectrometer (ULS2048 × 64) with an excitation wavelength of 405 nm in a N_2-filled glovebox. The SEM images were recorded using LEO Gemini 1530. The perovskite films were fabricated on the silicon substrate. The images were collected at a voltage of 0.1 kV. The film morphology was characterized by Bruker Dimension Icon FS AFM in tapping-mode at a resonant frequency of 300 kHz and a spring constant of 26 N m^{-1}. The root mean square (RMS) roughness values were extracted from images of 5 μm × 5 μm. Thin film thickness measurements were performed by a KLA Tencor Profilometer in air.

FET device measurement

All devices were characterized using Keithley 4200-SCS in a vacuum of 10^{-6} mbar. Transfer and output characteristics were operated in the pulsed mode and V_g was applied over a short pulse of 0.05 s during the scan. The temperature-dependent measurements were performed from 90 K to 295 K in a Janis probe station connected to a cryostat and cooled with liquid N_2. The temperature was monitored using thermocouples. Mobility values of FETs were extracted with the following equation: $\mu = \frac{2L}{WC_i}\left(\frac{\partial\sqrt{I_{ds}}}{\partial V_g}\right)^2$ where L, W, and C_i are the channel length and width and the unit capacitance of the oxide dielectric, respectively.[19]

Details of DFT calculations

Density functional theory (DFT) calculations were conducted using the Vienna *Ab initio* Simulation Package (VASP, version 6.1),[45] employing the PBE exchange–correlation functional.[46] The initial structure of the material was adapted from a similar Pb-based material reported by Lermer *et al.*,[47] which was subsequently optimized using the following protocol: to account for valence–core interactions, the projected augmented wave (PAW) method was employed.[48] During geometry relaxation, a plane-wave kinetic energy cutoff of 520 eV, an energy convergence threshold of 10^{-5} eV, and forces on each atom smaller than 0.01 eV Å^{-1} were used. Furthermore, van der Waals interactions were incorporated using Grimme's D3 method during the structure optimization.[49] For both structural relaxation and densities of states (DOS) calculations, we adopted Brillouin zone sampling with a Monkhorst–Pack 4 × 4 × 1 k-mesh. In all our calculations, the valence electron counts per atom type were as follows: Sn (14), I (7), C (4), H (1), N (5). Recognizing the importance of spin–orbit coupling (SOC) in understanding the electronic structure of hybrid organic/inorganic perovskite materials,[50] we considered SOC effects when performing DOS and band structure calculations. For the visualization and post-processing of structures, DOS, and band structures, we employed a combination of tools including VESTA,[51] VASPKIT,[52] and the *sumo* package.[53]

Optical pump-THz probe (OPTP) spectroscopy

The THz spectrometer is driven by a mode-locked Ti:Sappire laser with central wavelength of 800 nm, repetition rate of 1 kHz, and pulse duration of 50 fs. The output laser beam is separated for THz generation through optical rectification in a 1 mm-thick ZnTe crystal, and optical excitation. A photoexcitation with photon energy of 3.10 eV generated by a beta barium borate crystal was employed to generate charge carriers in the conduction and valence bands. Secondly, a single-cycle THz pulse with ~1 ps duration transmitted collinearly through the perovskite thin film on fused silica substrate interacting with the photoexcited electrons and holes. The photoconductivity $\Delta\sigma$ of these photogenerated charge carriers is directly probed by the THz pulse in the transmission geometry, and related to the relative attenuation of the THz peak field ($\Delta E = E_{pump} - E_0$, with E_{pump} and E_0 representing the transmitted THz peak field with and without excitations) based on the thin-film approximation. In principle, $\Delta\sigma$ can be expressed as: $\Delta\sigma = \Delta N \times e \times \mu$, with e and μ representing elementary charge and charge carrier mobility.[54] The free charge carrier density ΔN can be further related to the absorbed photon density N_{abs} and the photon-to-free-carrier quantum efficiency ϕ ($0 \le \phi \le 1$) following: $\Delta N = N_{abs} \times \phi$. Then the time dependent effective mobility is calculated from $\frac{\sigma}{N_{abs,flim}} = \left(-\frac{\varepsilon_0 c(n_1+n_2)}{d}\cdot\frac{\Delta E}{E}\right)\cdot\frac{d}{N_{abs}} = \varphi\mu$. Where n_1 = 1.96 is the THz refractive index of fused silica,

n_2 = 1 the refractive index of the air. $N_{ads,flim}$ is the number of absorbed photons in the unit thickness.[55]

Author contributions

S. L. W., T. M., and W. P. designed the concept and content of the experiment, L. G. performed THz spectra measurement with the support from H. I. W., M. M. performed DFT calculations and analyzed the data with help from D. A., H. W. synthesized and characterized the Bn organic spacer. Z. T. L. helped with data analysis for device measurement, M. B. and P. B. coordinated this work, T. M., and W. P. supervised the project, S. L. W. prepared the original manuscript with other co-authors. All authors discussed the results and commented on the manuscript.

Data availability

The data supporting this article have been included as part of the ESI.† Further relevant data are available from the corresponding author upon reasonable request.

Conflicts of interest

There are no conflicts to declare.

Acknowledgements

S. L. Wang and Z. Ling thank the China Scholarship Council (CSC, 201906890035 and 202006890007) for financial support. M. Mandal acknowledges postdoctoral support from the Alexander von Humboldt Foundation. D. Andrienko acknowledges funding of the Deutsche Forschungsgemeinschaft (DFG) Priority Program SPP2196, project 424708673 and the KAUST Office of Sponsored Research, grant OSR-CRG2020-4350. Open Access funding provided by the Max Planck Society.

References

1 H. Zhu, S. Teale, M. N. Lintangpradipto, S. Mahesh, B. Chen, M. D. McGehee and O. M. Bakr, *Nat. Rev. Mater.*, 2023, **8**, 569–586.
2 L. Ma, J. Dai and X. C. Zeng, *Adv. Energy Mater.*, 2017, **7**, 7.
3 Q. Zhang, Q. Shang, R. Su, T. T. H. Do and Q. Xiong, *Nano Lett.*, 2021, **21**, 1903–1914.
4 F. Paulus, C. Tyznik, O. D. Jurchescu and Y. Vaynzof, *Adv. Funct. Mater.*, 2021, **31**, 2101029.
5 X. Liu, D. Yu, X. Song and H. Zeng, *Small*, 2018, **14**, 1801460.
6 B. Jeong, L. Veith, T. J. Smolders, M. J. Wolf and K. Asadi, *Adv. Mater.*, 2021, **33**, 2100486.
7 W. Yu, F. Li, L. Yu, M. R. Niazi, Y. Zou, D. Corzo and A. Amassian, *Nat. Commun.*, 2018, **9**, 5354.
8 N. D. Canicoba, N. Zagni, F. Liu, G. McCuistian, K. Fernando, H. Bellezza and A. D. Mohite, *ACS Mater. Lett.*, 2019, **1**, 633–640.
9 S. Zhou, Y. Ma, G. Zhou, X. Xu, M. Qin, Y. Li and X. Lu, *ACS Energy Lett.*, 2019, **4**, 534–541.
10 C. Ma, S. Clark, Z. Liu, L. Liang, Y. Firdaus, R. Tao and T. Wu, *ACS Nano*, 2020, **14**, 3969–3979.
11 S. Wang, K. Bidinakis, C. Haese, F. H. Hasenburg, O. Yildiz, Z. Ling, M. Bonn, P. W. M. Blom, H. I. Wang, W. Pisula and T. Marszalek, *Small*, 2023, **19**, 2207426.
12 Y. Zheng, T. Niu, X. Ran, J. Qiu, B. Li, Y. Xia and W. Huang, *J. Mater. Chem. A*, 2019, **7**, 13860–13872.
13 H. Zhu, A. Liu, K. I. Shim, J. Hong, J. W. Han and Y. Y. Noh, *Adv. Mater.*, 2020, **32**, 2002717.
14 C. Qin, F. Zhang, L. Qin, X. Liu, H. Ji, L. Li and F. Teng, *Adv. Electron. Mater.*, 2021, **7**, 2100384.
15 Y. Fu, X. Jiang, X. Li, B. Traore, I. Spanopoulos, C. Katan and E. Harel, *J. Am. Chem. Soc.*, 2020, **142**, 4008–4021.
16 Q. Yang, W. Fang, S. Wang, Y. Gu, X. Bi, K. Diao and B. Liu, *Sol. Energy Mater. Sol. Cells*, 2023, **261**, 112511.
17 S. Wang, M. Mandal, H. Zhang, D. W. Breiby, O. Yildiz, Z. Ling, M. Bonn, P. W. M. Blom, H. I. Wang, W. Pisula and T. Marszalek, *J. Am. Chem. Soc.*, 2024, **146**, 19128–19136.
18 Y. Gao, Z. Wei, P. Yoo, E. Shi, M. Zeller, C. Zhu and L. Dou, *J. Am. Chem. Soc.*, 2019, **141**, 15577–15585.
19 S. Wang, S. Frisch, H. Zhang, O. Yildiz, M. Mandal, N. Ugur, M. Bonn, P. W. M. Blom, H. I. Wang, W. Pisula and T. Marszalek, *Mater. Horiz.*, 2022, **9**, 2633–2643.
20 S. Wang, S. Kalyanasundaram, L. Gao, Z. Ling, Z. Zhou, M. Bonn, P. W. M. Blom, H. I. Wang, W. Pisula and T. Marszalek, *Mater. Horiz.*, 2024, **11**, 1177–1187.
21 S. H. Reddy, F. Di Giacomo and A. Di Carlo, *Adv. Energy Mater.*, 2022, **12**, 2103534.
22 X. J. She, C. Chen, G. Divitini, B. Zhao, Y. Li, J. Wang and H. Sirringhaus, *Nat. Electron.*, 2020, **3**, 694–703.
23 I. Zimmermann, S. Aghazada and M. K. Nazeeruddin, *Angew. Chem., Int. Ed.*, 2019, **131**, 1084–1088.
24 M. Dyksik, H. Duim, X. Zhu, Z. Yang, M. Gen, Y. Kohama, S. Adjokatse, D. K. Maude, M. A. Loi, D. A. Egger and M. Baranowski, *ACS Energy Lett.*, 2020, **5**, 3609–3616.
25 P. Peksa, A. Maufort, M. Baranowski, A. Surrente, L. Lutsen, P. Płochocka, W. T. Van Gompel and M. Dyksik, *J. Phys. Chem. C*, 2024, **128**, 17984–17989.
26 R. Wang, Y. Tong, K. Wang, S. Xia, E. Kentzinger, O. Soltwedel and H. Frielinghaus, *Nanoscale Horiz.*, 2019, **4**, 1139–1144.
27 S. Sidhik, Y. Wang, M. De Siena, R. Asadpour, A. J. Torma, T. Terlier and A. D. Mohite, *Science*, 2022, **377**, 1425–1430.
28 B. Cheng and Q. Q. Chu, *Matter*, 2022, **5**, 4110–4111.
29 R. Liu and K. Xu, *Micro Nano Lett.*, 2020, **15**, 349–353.
30 Y. Liang, Q. Shang, M. Li, S. Zhang, X. Liu and Q. Zhang, *Adv. Funct. Mater.*, 2021, **31**, 2106108.
31 J. Qiu, Y. Zheng, Y. Xia, L. Chao, Y. Chen and W. Huang, *Adv. Funct. Mater.*, 2019, **29**, 1806831.
32 J. Yuan, Y. Jiang, T. He, G. Shi, Z. Fan and M. Yuan, *Sci. China: Chem.*, 2019, **62**, 629–636.
33 F. Li, J. Zhang, S. Jo, M. Qin, Z. Li, T. Liu and A. K. Y. Jen, *Small Methods*, 2020, **4**, 1900831.

34 Z. Wang, F. Wang, B. Zhao, S. Qu, T. Hayat, A. Alsaedi and Z. A. Tan, *J. Phys. Chem. Lett.*, 2020, **11**, 1120–1127.
35 A. L. Alvarado-Leanos, D. Cortecchia, C. N. Saggau, S. Martani, G. Folpini, E. Feltri and A. Petrozza, *ACS Nano*, 2022, **16**, 20671–20679.
36 F. Zhang, Q. Zhang, X. Liu, Y. Hu, Z. Lou, Y. Hou and F. Teng, *ACS Appl. Mater. Interfaces*, 2021, **13**, 24272–24284.
37 J. Wang, H. Shen, W. Li, S. Wang, J. Li and D. Li, *Adv. Sci.*, 2019, **6**, 1802019.
38 H. Wan, Y. Cao, L. W. Lo, J. Zhao, N. Sepulveda and C. Wang, *ACS Nano*, 2020, **14**, 10402–10412.
39 S. P. Senanayak, M. Abdi-Jalebi, V. S. Kamboj, R. Carey, R. Shivanna, T. Tian and H. Sirringhaus, *Sci. Adv.*, 2020, **6**, 4948.
40 P. Mathew, J. Cho and P. V. Kamat, *ACS Energy Lett.*, 2024, **9**, 1103–1114.
41 S. P. Senanayak, B. Yang, T. H. Thomas, N. Giesbrecht, W. Huang, E. Gann, B. Nair, K. Goedel, S. Guha, X. Moya, C. R. McNeill and H. Sirringhaus, *Sci. Adv.*, 2017, **3**, 1601935.
42 H. Zhang, E. Debroye, J. A. Steele, M. B. Roeffaers, J. Hofkens, H. I. Wang and M. Bonn, *ACS Energy Lett.*, 2021, **6**, 568–573.
43 S. G. Motti, M. Kober-Czerny, M. Righetto, P. Holzhey, J. Smith, H. Kraus, H. J. Snaith, M. B. Johnston and L. M. Herz, *Adv. Funct. Mater.*, 2023, **33**, 2300363.
44 L. Gao, H. Zhang, Y. Zhang, S. Fu, J. J. Geuchies, D. Valli and M. Bonn, *Adv. Mater.*, 2024, **36**, 2406109.
45 G. Kresse and J. Furthmüller, *Phys. Rev. B: Condens. Matter Mater. Phys.*, 1996, **54**, 11169.
46 J. P. Perdew, K. Burke and M. Ernzerhof, *Phys. Rev. Lett.*, 1996, 77, 3865.
47 C. Lermer, S. P. Harm, S. T. Birkhold, J. A. Jaser, C. M. Kutz, P. Mayer and B. V. Lotsch, *Z. Anorg. Allg. Chem.*, 2016, **642**, 1369–1376.
48 G. Kresse and J. Furthmüller, *Comput. Mater. Sci.*, 1996, **6**, 15–50.
49 G. Kresse and D. Joubert, *Phys. Rev. B: Condens. Matter Mater. Phys.*, 1999, **59**, 1758.
50 S. Grimme, J. Antony, S. Ehrlich and H. Krieg, *J. Chem. Phys.*, 2010, **132**, 154104.
51 K. Momma and F. Izumi, *J. Appl. Crystallogr.*, 2011, **44**, 1272–1276.
52 V. Wang, N. Xu, J. C. Liu, G. Tang and W. T. Geng, *Comput. Phys. Commun.*, 2021, **267**, 108033.
53 A. M. Ganose, A. J. Jackson and D. O. Scanlon, *J. Open Source Softw.*, 2018, **3**, 717.
54 X. Ai, M. C. Beard, K. P. Knutsen, S. E. Shaheen, G. Rumbles and R. J. Ellingson, *J. Phys. Chem. B*, 2006, **110**, 25462–25471.
55 P. D. Cunningham and L. M. Hayden, *J. Phys. Chem. C*, 2008, **112**, 7928–7935.